



# Thermal boundary conditions for thermal lattice Boltzmann simulations

Chih-Hao Liu, Kuen-Hau Lin, Hao-Chueh Mai, Chao-An Lin\*

Department of Power Mechanical Engineering, National Tsing Hua University, Hsinchu 30013, Taiwan

## ARTICLE INFO

### Keywords:

Thermal boundary conditions  
Thermal lattice Boltzmann simulations  
Macroscopic energy equation  
Wall  
Corner

## ABSTRACT

Consistent 2D and 3D thermal boundary conditions for thermal lattice Boltzmann simulations are proposed. The boundary unknown energy distribution functions are made functions of known energy distribution functions and correctors, where the correctors at the boundary nodes are obtained directly from the definition of internal energy density. This boundary condition can be easily implemented on the wall and corner boundary using the same formulation. The discrete macroscopic energy equation is also derived for a steady and fully developed channel flow to assess the effect of the boundary condition on the solutions, where the resulting second order accurate central difference equation predicts continuous energy distribution across the boundary, provided the boundary unknown energy distribution functions satisfy the macroscopic energy level. Four different local known energy distribution functions are experimented with to assess both this observation and the applicability of the present formulation, and are scrutinized by calculating the 2D thermal Poiseuille flow, thermal Couette flow, thermal Couette flow with wall injection, natural convection in a square cavity, and 3D thermal Poiseuille flow in a square duct. Numerical simulations indicate that the present formulation is second order accurate and the difference of adopting different local known energy distribution functions is, as expected, negligible, which are consistent with the results from the derived discrete macroscopic energy equation.

© 2009 Elsevier Ltd. All rights reserved.

## 1. Introduction

The lattice Boltzmann method (LBM) [1–3] has been successfully applied to various isothermal hydrodynamic problems. The major advantages of the LBM are that it is explicit, easy to implement, and natural to parallelize. However, its application to the non-isothermal problem is limited because of the numerical instability of thermal models [4]. In general, the thermal lattice Boltzmann model (TLBM) can be categorized into two types [5]. The first one is the multi-speed approach and the second one is the passive scalar model. The major advantage of the passive scalar model over the multi-speed approach is the enhancement of numerical stability, and thus the former is commonly adopted. It should be noted that the stability of the thermal model can be further enhanced by adopting the hybrid finite-difference approach [6,7].

In the passive scalar thermal lattice Boltzmann models [5,8,9], a separate distribution function is used to solve for the temperature distribution. For example, the evolution scheme proposed by He et al. [5] was introduced to simulate thermal flows. This model has a better numerical stability than the multi-speed approach, and the viscous heat dissipation and the compression work done by the pressure can be solved implicitly. Peng et al. [8] proposed a simplified thermal energy distribution model where the compression work done by the pressure and viscous heat dissipation are neglected. By introducing a forcing function, Guo et al. [9] proposed a thermal lattice BGK equation with viscous heat dissipation in the incompressible limit.

\* Corresponding author.

E-mail address: [calin@pme.nthu.edu.tw](mailto:calin@pme.nthu.edu.tw) (C.-A. Lin).

However, a successful TLBM simulation similar to its isothermal counterpart rests on the correct implementation of boundary conditions, where unknown populations originated from the undefined nodes external to the flow domain are encountered during the streaming operation. For isothermal flow, the bounce-back scheme is the most popular method to handle stationary no slip wall boundaries, but it has been confirmed that the bounce-back scheme is only of first order accurate [10], which degrades the second order accuracy of the lattice Boltzmann equation (LBE). Other boundary treatments have been developed to improve the numerical accuracy of the LBE [11–14]. For D2Q7 lattice, the unknown distribution functions at the plane boundary node can be obtained directly from the definitions of density and momentum [11]. For D2Q9 and D3Q15 lattice models, the numbers of unknown distribution functions exceed the number of constraint equations, therefore extra constraints [13], though different formulations in 2D and 3D, were adopted [14]. To remedy this inconsistency, Chang et al. [15] and Ho et al. [16] proposed a consistent boundary condition that unknown density distributions are made functions of local known density distributions and correctors, where the same formulation can be applied to 2D and 3D velocity and mixed pressure–velocity boundaries. Also, a multi-reflection approach to model Dirichlet and Neumann time-dependent boundary conditions for arbitrarily shaped surfaces was proposed Ginzburg and co-workers [17,18].

As for the thermal boundary conditions, He et al. [5] extended the bounce-back rule of nonequilibrium distributions proposed by Zou and He [14] to impose thermodynamic boundary conditions. Also similar to the counter-slip approach of Inamuro [12], D’Orazio et al. [19] proposed that the incoming unknown thermal populations are assumed to be equilibrium distributions with a counter-slip thermal energy. While in Tang et al. [20], the unknown energy distribution at the boundary node is decomposed into equilibrium and nonequilibrium parts. The nonequilibrium part is approximated with a first order extrapolation of the nonequilibrium part of populations at the neighboring domain nodes.

In this paper, alternate but also consistent thermal boundary conditions for 2D and 3D thermal lattice Boltzmann simulations are presented. The unknown energy distributions are made functions of local known energy distributions and correctors. The correctors at the boundary nodes are obtained directly from the definition of internal energy density. This thermal boundary condition is an extended form of the hydrodynamic boundary conditions proposed in [15,16]. To assess the effect of the boundary condition on the solutions, discrete macroscopic energy equation is also derived for a steady and fully developed channel flow. The validity and accuracy of this new thermal boundary condition are scrutinized by computing the 2D thermal Poiseuille flow, thermal Couette flow, thermal Couette flow with wall injection, and natural convection in a square cavity. Moreover, to validate its consistent formulation to 3D problems, a 3D thermal Poiseuille flow in a square duct is also simulated. Analytic and benchmark solutions are used to examine the accuracy of the boundary conditions.

## 2. Thermal lattice Boltzmann models

The thermal lattice Boltzmann equations [8] adopting a uniform lattice with BGK collision model can be expressed as,

$$f_i(\vec{x} + \vec{e}_i \Delta t, t + \Delta t) = f_i(\vec{x}, t) - \frac{1}{\tau_f} [f_i(\vec{x}, t) - f_i^{eq}(\vec{x}, t)] \quad (1)$$

$$g_i(\vec{x} + \vec{e}_i \Delta t, t + \Delta t) = g_i(\vec{x}, t) - \frac{1}{\tau_g} [g_i(\vec{x}, t) - g_i^{eq}(\vec{x}, t)] \quad (2)$$

where  $f_i$  and  $g_i$  are the particle density and energy distribution functions along the particle velocity direction  $\vec{e}_i$ , respectively.  $\tau_f$  and  $\tau_g$  are the dimensionless relaxation times that control the rates approaching equilibrium.

Here, the macroscopic variables are defined as:

$$\rho = \sum_i f_i \quad (3)$$

$$\rho \vec{u} = \sum_i f_i \vec{e}_i \quad (4)$$

$$\rho \frac{1}{2} D_0 R T = \sum_i g_i \quad (5)$$

where  $D_0$  is the number of degrees of freedom of a particle and  $R$  is the ideal gas constant.

For the present 2D and 3D applications, D2Q9 and D3Q19 models are adopted. The equilibrium density distribution functions for these two models are

$$f_i^{eq} = \omega_i \rho \left[ 1 + \frac{3\vec{e}_i \cdot \vec{u}}{C^2} + \frac{9(\vec{e}_i \cdot \vec{u})^2}{2C^4} - \frac{3\vec{u} \cdot \vec{u}}{2C^2} \right] \quad (6)$$

where the weighting factors  $\omega_i$  are  $\omega_0 = 4/9$ ,  $\omega_{i=1-4} = 1/9$ ,  $\omega_{i=5-8} = 1/36$ , and  $\omega_0 = 1/3$ ,  $\omega_{i=1-6} = 1/18$ ,  $\omega_{i=7-18} = 1/36$  for D2Q9 and D3Q19 models, respectively.

For the D2Q9 model, the particle velocity  $\vec{e}_i$  is defined as,

$$\vec{e}_i = \begin{cases} (0, 0)C, & i = 0 \\ (\cos[(i-1)\pi/2], \sin[(i-1)\pi/2])C, & i = 1-4 \\ (\cos[(2i-9)\pi/4], \sin[(2i-9)\pi/4])\sqrt{2}C, & i = 5-8. \end{cases} \quad (7)$$

The equilibrium energy distribution functions, which depend on the local macroscopic variables, are given as [5,8]

$$\begin{aligned} g_0^{eq} &= -\frac{2}{3}\rho\varepsilon \frac{\vec{u} \cdot \vec{u}}{C^2} \\ g_{1-4}^{eq} &= \frac{1}{9}\rho\varepsilon \left[ \frac{3}{2} + \frac{3\vec{e}_i \cdot \vec{u}}{2C^2} + \frac{9(\vec{e}_i \cdot \vec{u})^2}{2C^4} - \frac{3\vec{u} \cdot \vec{u}}{2C^2} \right] \\ g_{5-8}^{eq} &= \frac{1}{36}\rho\varepsilon \left[ 3 + \frac{6\vec{e}_i \cdot \vec{u}}{C^2} + \frac{9(\vec{e}_i \cdot \vec{u})^2}{2C^4} - \frac{3\vec{u} \cdot \vec{u}}{2C^2} \right] \end{aligned} \quad (8)$$

where the internal energy  $\varepsilon = \frac{1}{2}D_0RT$ . Here,  $C = \Delta x/\Delta t$  is the lattice speed, where  $\Delta x$  and  $\Delta t$  are the lattice width and time step, respectively. The corresponding kinematic viscosity and thermal diffusivity are calculated by  $\nu = (\tau_f - 0.5)C_s^2\Delta t$  and  $\chi = 2(\tau_g - 0.5)C_s^2\Delta t$  [8], where  $C_s = \sqrt{RT} = C/\sqrt{3}$  is the speed of sound.

For the D3Q19 model, the particle velocity  $\vec{e}_i$  is defined as,

$$\vec{e}_i = \begin{cases} (0, 0, 0)C, & i = 0 \\ (\pm 1, 0, 0)C, (0, \pm 1, 0)C, (0, 0, \pm 1)C, & i = 1-6 \\ (\pm 1, \pm 1, 0)C, (0, \pm 1, \pm 1)C, (\pm 1, 0, \pm 1)C, & i = 7-18. \end{cases} \quad (9)$$

The equilibrium energy distribution functions can be expressed as [5,8],

$$\begin{aligned} g_0^{eq} &= -\frac{1}{2}\rho\varepsilon \frac{\vec{u} \cdot \vec{u}}{C^2} \\ g_{1-6}^{eq} &= \frac{1}{18}\rho\varepsilon \left[ 1 + \frac{\vec{e}_i \cdot \vec{u}}{C^2} + \frac{9(\vec{e}_i \cdot \vec{u})^2}{2C^4} - \frac{3\vec{u} \cdot \vec{u}}{2C^2} \right] \\ g_{7-18}^{eq} &= \frac{1}{36}\rho\varepsilon \left[ 2 + \frac{4\vec{e}_i \cdot \vec{u}}{C^2} + \frac{9(\vec{e}_i \cdot \vec{u})^2}{2C^4} - \frac{3\vec{u} \cdot \vec{u}}{2C^2} \right]. \end{aligned} \quad (10)$$

Here, the corresponding kinematic viscosity and thermal diffusivity are given by  $\nu = (\tau_f - 0.5)C_s^2\Delta t$  and  $\chi = 5(\tau_g - 0.5)C_s^2\Delta t/3$  [21], respectively.

Following the procedure in [9], the viscous heat dissipation and compression work done by the pressure can be naturally incorporated by adding a viscous heat dissipation term  $\phi_i$  to Eq. (2), that is,

$$g_i(\vec{x} + \vec{e}_i\Delta t, t + \Delta t) = g_i(\vec{x}, t) - \frac{1}{\tau_g}[g_i(\vec{x}, t) - g_i^{eq}(\vec{x}, t)] + \phi_i(\vec{x}, t) \quad (11)$$

where the final discrete form of this viscous heat dissipation term can be expressed as,

$$\phi_i = -(f_i - f_i^{eq})(\vec{e}_i - \vec{u})(\vec{e}_i - \vec{u}) : \frac{\partial \vec{u}}{\partial \vec{x}}. \quad (12)$$

Including this term will lead to a change in the thermal diffusivity  $\chi$  for the D2Q9 model, from  $2(\tau_g - 0.5)C_s^2\Delta t$  to  $(\tau_g - 0.5)C_s^2\Delta t$  [9].

### 3. Discrete forms of the macroscopic momentum and temperature equations

Before proceeding to the discussions of the boundary conditions of the lattice Boltzmann methods, it is beneficial here to derive first the discrete forms of the macroscopic momentum and temperature equations based on the lattice Boltzmann equations, i.e. Eq. (1), (2) and (6), (8). Since general discrete forms are difficult to derive, the focus here is on the D2Q9 steady fully developed channel flow driven by a fixed body force ( $G$ ) with periodic boundary conditions.

The discrete Navier–Stokes equation for a steady and fully developed channel flow has been derived by He et al. [10] and is expressed as,

$$\begin{aligned} \frac{u_{j+1}v_{j+1} - u_{j-1}v_{j-1}}{2\delta x} &= \underbrace{\frac{2\tau - 1}{6} \frac{\delta x^2}{\delta t}}_{\nu} \frac{u_{j-1} - 2u_j + u_{j+1}}{\delta x^2} + G \\ &+ \frac{\tau - 1}{\delta t} [\mathbf{u}_{j-1} - u_{j-1} + \mathbf{u}_{j+1} - u_{j+1}] - \frac{2\tau^2 - 2\tau + 1}{\tau\delta t} [\mathbf{u}_j - u_j] \end{aligned} \quad (13)$$

where  $u$  and  $v$  are streamwise and transverse velocity, respectively and  $j$  is the discrete index in the transverse direction. It should be noted, however, that  $\mathbf{u}$  and  $u$  are defined in Eqs. (4) and (6), respectively. Except in the boundary,  $\mathbf{u} = u$ . Thus the equation reduces to the second order accurate central difference equation. For a steady and fully developed channel flow without transverse wall injection ( $v = 0$ ), the equation predicts exact parabolic profiles.

The influence of the boundary condition can be verified by considering the above equation next to the lower wall, i.e.

$$\frac{u_3 v_3 - u_1 v_1}{2\delta x} = \underbrace{\frac{2\tau - 1}{6} \frac{\delta x^2}{\delta t}}_v \frac{u_1 - 2u_2 + u_3}{\delta x^2} + G + \frac{\tau - 1}{\delta t} [\mathbf{u}_1 - u_1] \quad (14)$$

where index  $j = 1$  locates the lower wall.  $u_1$  is no slip wall velocity and  $\mathbf{u}_1$  is computed by the wall distribution function, i.e.  $\rho \mathbf{u}_1 = C(f_1^{j=1} + f_5^{j=1} + f_8^{j=1} - f_3^{j=1} - f_6^{j=1} - f_7^{j=1})$ . It is clear that  $f_2^{j=1}$ ,  $f_5^{j=1}$  and  $f_6^{j=1}$  are to be determined at the wall. He et al. [10] concluded that, slip velocity is zero as long as  $\mathbf{u}_1 = u_1$  regardless of the formulation of  $f_2^{j=1}$ ,  $f_5^{j=1}$  and  $f_6^{j=1}$ . This provides a guide to determine the unknown density population at the wall to be addressed in the next section. Also, since Eq. (14) involves one inhomogeneous direction only, therefore further numerical tests are adopted to assess whether this assertion is still valid for flows with two inhomogeneous directions.

Using similar technique, the discrete temperature equation can be derived for fully developed channel flow. Here, for simplicity, the body force is neglected. Using Eqs. (2) and (8), the result is,

$$\begin{aligned} \frac{T_{j+1} v_{j+1} - T_{j-1} v_{j-1}}{2\delta x} &= \underbrace{\frac{2\tau - 1}{3} \frac{\delta x^2}{\delta t}}_x \frac{T_{j-1} - 2T_j + T_{j+1}}{\delta x^2} + \chi \frac{3}{2c^2} \frac{T_{j-1} v_{j-1}^2 - 2T_j v_j^2 + T_{j+1} v_{j+1}^2}{\delta x^2} \\ &+ \frac{\tau - 1}{\delta t} [T_{j-1} - T_{j-1} + T_{j+1} - T_{j+1}] - \frac{2\tau^2 - 2\tau + 1}{\tau \delta t} [T_j - T_j]. \end{aligned} \quad (15)$$

Again, if the temperature ( $\mathbf{T}$ ) defined by the distribution function Eq. (5) is the same as that ( $T$ ) used in the equilibrium distribution function Eq. (8), then the equation reduces to the second order accurate central difference equation. It is noted that the second diffusion like term is smaller than the first diffusion term by a factor of  $Ma^2$  and is negligible for low Mach number flow.

The influence of the thermal boundary condition can be verified by considering the above equation next to the lower wall, i.e.

$$\frac{T_3 v_3 - T_1 v_1}{2\delta x} = \underbrace{\frac{2\tau - 1}{3} \frac{\delta x^2}{\delta t}}_x \frac{T_1 - 2T_2 + T_3}{\delta x^2} + \chi \frac{3}{2c^2} \frac{T_1 v_1^2 - 2T_2 v_2^2 + T_3 v_3^2}{\delta x^2} + \frac{\tau - 1}{\delta t} [T_1 - T_1] \quad (16)$$

where  $T_1$  is the wall temperature and  $\mathbf{T}_1$  is determined by the energy distribution function, i.e.  $\rho R \mathbf{T}_1 = g_0^{j=1} + g_1^{j=1} + g_2^{j=1} + g_3^{j=1} + g_4^{j=1} + g_5^{j=1} + g_6^{j=1} + g_7^{j=1} + g_8^{j=1}$ . It is clear that  $g_2^{j=1}$ ,  $g_5^{j=1}$ ,  $g_6^{j=1}$  are to be determined at the wall. Similar to the momentum equation, the above equation produces correct answer as long as  $\mathbf{T}_1 = T_1$ . This provides a guide to determine the unknown energy distribution population at the wall to be addressed in the next section.

#### 4. Hydrodynamic boundary conditions

Boundary condition proposed in [15,16] is employed to determine the unknown particle density distribution functions along the boundary, which are expressed as a combination of the local known value and a corrector,

$$f_i(\vec{x}, t) = f_i^*(\vec{x}, t) + \frac{\omega_i}{C} \vec{e}_i \cdot \vec{Q} \quad (17)$$

where  $\vec{Q}$  is the force like corrector to enforce the required momentum. This resembles the modification of momentum due to the presence of a body force, though this only applies to the unknown particle density distribution functions along the boundary. This formulation is similar to that proposed by Maier et al. [13] for determining the velocity boundary conditions, though with slight variation. However, as will be shown next, the present formulation can be equally applied to velocity or mixed pressure-velocity boundary and even corner for 2D and 3D flows.

For instance, consider a node at the left boundary as shown in Fig. 1, where the unknown density distribution functions are  $f_1, f_5$  and  $f_8$ , i.e.  $f_1 = f_1^* + \omega_1 Q_x$ ,  $f_5 = f_5^* + \omega_5 (Q_x + Q_y)$ , and  $f_8 = f_8^* + \omega_8 (Q_x - Q_y)$ . Therefore, the macroscopic velocity and density at the node using Eqs. (3) and (4), in conjunction with Eq. (17), can be expressed as,

$$\rho = f_0 + [f_1^* + \omega_1 Q_x] + f_2 + f_3 + f_4 + [f_5^* + \omega_5 (Q_x + Q_y)] + f_6 + f_7 + [f_8^* + \omega_8 (Q_x - Q_y)] \quad (18)$$

$$\rho u = (f_1^* + \omega_1 Q_x) + [f_5^* + \omega_5 (Q_x + Q_y)] + [f_8^* + \omega_8 (Q_x - Q_y)] - f_3 - f_6 - f_7 \quad (19)$$

$$\rho v = f_2 + [f_5^* + \omega_5 (Q_x + Q_y)] + f_6 - f_4 - f_7 - [f_8^* + \omega_8 (Q_x - Q_y)]. \quad (20)$$

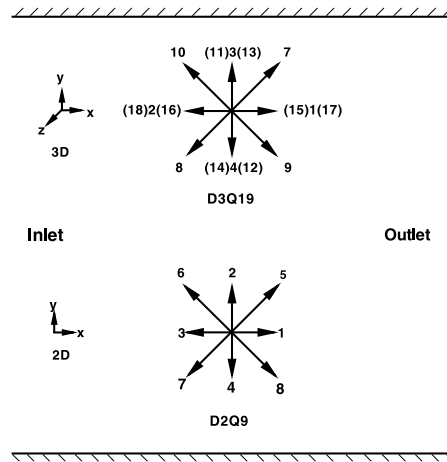


Fig. 1. The 2D and 3D models.

If velocities  $u$  and  $v$  are known at the boundary, Eqs. (18) to (20) can be used to solve for  $\rho$ ,  $Q_x$ , and  $Q_y$ , and then  $f_4, f_7$ , and  $f_8$  are obtained. The explicit forms of the unknown particle density distribution functions are shown as below.

$$\rho = \frac{1}{1+u} [f_0 + f_2 + f_4 + 2(f_3 + f_6 + f_7)]$$

$$f_1 = f_1^* + \frac{2}{3}\rho u + \frac{2}{3}(f_3 - f_1^* + f_7 - f_5^* + f_6 - f_8^*) \quad (21)$$

$$f_5 = f_5^* + \frac{1}{6}\rho u + \frac{1}{2}\rho v - \frac{1}{2}(f_2 - f_4) + \frac{1}{6}(f_3 - f_1^*) + \frac{2}{3}(f_7 - f_5^*) - \frac{1}{3}(f_6 - f_8^*) \quad (22)$$

$$f_8 = f_8^* + \frac{1}{6}\rho u - \frac{1}{2}\rho v + \frac{1}{2}(f_2 - f_4) + \frac{1}{6}(f_3 - f_1^*) - \frac{1}{3}(f_7 - f_5^*) + \frac{2}{3}(f_6 - f_8^*). \quad (23)$$

The local known  $f_i^*$  is still yet to be decided. Ho et al. [16], experimented three different forms of  $f^*$ , i.e. (a) :  $f_i^*(\vec{x}, t) = f(\vec{x}, -\vec{e}_i, t)$ , (b) :  $f_i^*(\vec{x}, t) = f(\vec{x}, \vec{e}_i, t - dt)$  and (c) :  $f_i^*(\vec{x}, t) = f^{eq}(\vec{x}, \vec{e}_i, t)$ , and differences are observed to be negligible. This seems to suggest in the present formulation by satisfying the momentum, the influence of the choice of the local known distribution function  $f^*$  is negligible. This is also confirmed from the macroscopic equation shown in Eq. (14) and in [10]. Other forms can also be employed. For example in Chang et al. [15], to simulate flow with an immersed object, the local unknown distribution functions around the immersed object was assumed to be the distribution functions streaming from the upstream directions from the immersed object. For formulation (a), the present form recovers the form by Zou and He [14], and is adopted here.

Another type of boundary condition is frequently encountered, i.e. pressure  $\rho$  and transverse velocity  $v$  are prescribed. If velocities  $v$  and  $\rho$  are known at the boundary, Eqs. (18) to (20) can be used to solve for the three unknowns, namely  $Q_x$  and  $Q_y$ , which are then used to update the unknown particle distribution functions  $f_i(\vec{x}, t)$  along the boundary and obtain  $u$ . The explicit form of the unknown particle distribution functions are shown below.

$$u = 1 - \frac{f_0 + f_2 + f_4 + 2(f_3 + f_6 + f_7)}{\rho} \quad (24)$$

where  $f_1, f_5$  and  $f_8$  are the same as those in Eqs. (21) to (23).

The present boundary condition can be applied to the corner nodes. Consider the top left corner node (Fig. 1) of a 2D domain, where the unknown distribution functions are  $f_1, f_4, f_5, f_7$  and  $f_8$ . It is clear that the distribution functions  $f_5$  and  $f_7$  do not stream from and into the flow domain, but it contributes to the level of the density. Therefore, the density at this location must be specified. Here for simplicity,  $f_i^*(\vec{x}, \vec{e}_i, t) = f_i(\vec{x}, -\vec{e}_i, t)$  is adopted and similar procedure can be applied to other schemes. Thus, the unknown distribution functions adopting Eq. (17) are expressed as  $f_1 = f_3 + \omega_1 Q_x$ ,  $f_4 = f_2 - \omega_4 Q_y$ ,  $f_5 = f_7 + \omega_5(Q_x + Q_y)$  and  $f_8 = f_6 + \omega_8(Q_x - Q_y)$ .  $f_7$  is solved as part of the solution to avoid recursive computation, but  $f_7 = f_5 - \omega_7(Q_x + Q_y)$  is still valid. Now, for known  $\rho$ ,  $u$  and  $v$ , then

$$\begin{aligned} f_7 &= \frac{\rho - \rho u + \frac{2}{3}\rho v - f_0 - 2(f_2 + f_3 + f_6)}{2} \\ f_1 &= f_3 + \frac{2}{3}\rho u, \quad f_4 = f_2 - \frac{2}{3}\rho v \\ f_5 &= f_7 + \frac{1}{6}\rho u + \frac{1}{6}\rho v, \quad f_8 = f_6 + \frac{1}{6}\rho u + \frac{1}{6}\rho v. \end{aligned} \quad (25)$$

As expected, for a stationary wall, i.e.  $u = v = 0$ , this result is the same as that proposed by Zou and He [14]. However, the present method can be applied to non-stationary corners. Similar treatments can be applied to other corners for 2D and 3D flows.

## 5. Thermal boundary conditions

Here, similar to its hydrodynamic counterpart, a consistent thermal boundary condition is introduced. The unknown particle energy distribution function at the plane boundary is assumed to be

$$g_i(\vec{x}, t) = g_i^*(\vec{x}, t) + \omega_i G_c \quad (26)$$

where  $G_c$  is the correction to enforce the internal energy.

### 5.1. Dirichlet thermal boundary conditions

For instance, consider a node at the top boundary as shown in Fig. 1, where the unknown particle energy distribution functions are  $(g_4, g_7, g_8)$  and  $(g_4, g_8, g_9, g_{12}, g_{14})$ , respectively for D2Q9 and D3Q19 models. Therefore, the internal energy density at the node using Eq. (5), in conjunction with Eq. (26), can be expressed as, For the D2Q9 model,

$$\rho\varepsilon = g_0 + g_1 + g_2 + g_3 + [g_4^* + \omega_4 G_c] + g_5 + g_6 + [g_7^* + \omega_7 G_c] + [g_8^* + \omega_8 G_c] \quad (27)$$

$$\rho\varepsilon^* = g_0 + g_1 + g_2 + g_3 + g_4^* + g_5 + g_6 + g_7^* + g_8^* \quad (28)$$

$$G_c = \frac{\rho\varepsilon - \rho\varepsilon^*}{\omega_4 + \omega_7 + \omega_8}. \quad (29)$$

For the D3Q19 model,

$$\rho\varepsilon = g_0 + g_1 + g_2 + g_3 + [g_4^* + \omega_4 G_c] + g_5 + g_6 + g_7 + [g_8^* + \omega_8 G_c] + [g_9^* + \omega_9 G_c] + g_{10} + g_{11} + [g_{12}^* + \omega_{12} G_c] + g_{13} + [g_{14}^* + \omega_{14} G_c] + g_{15} + g_{16} + g_{17} + g_{18} \quad (30)$$

$$\rho\varepsilon^* = g_0 + g_1 + g_2 + g_3 + g_4^* + g_5 + g_6 + g_7 + g_8^* + g_9^* + g_{10} + g_{11} + g_{12}^* + g_{13} + g_{14}^* \quad (31)$$

$$G_c = \frac{\rho\varepsilon - \rho\varepsilon^*}{\omega_4 + \omega_8 + \omega_9 + \omega_{12} + \omega_{14}}. \quad (32)$$

If temperature  $T$  is known at the boundary, the corresponding internal energy  $\varepsilon = D_0 RT/2$  can be calculated with  $D_0$  being equal to 2 and 3 for 2D and 3D geometries, respectively. Hence  $(g_4, g_7, g_8)$  and  $(g_4, g_8, g_9, g_{12}, g_{14})$  are obtained for D2Q9 and D3Q19 models using Eq. (26) and  $G_c$ .

Again, the local known energy distribution function  $g_i^*(\vec{x}, t)$  is yet to be determined. By reference to Eq. (16), it should be anticipated that the choices should be irrelevant. Here, four different formulations of  $g_i^*$  are experimented with to validate the assertion, i.e.

$$\text{SchemeA : } g_i^*(\vec{x}, t) = g(\vec{x}, -\vec{e}_i, t) \quad (33)$$

$$\text{SchemeB : } g_i^*(\vec{x}, t) = g(\vec{x}, \vec{e}_i, t - \Delta t) \quad (34)$$

$$\text{SchemeC : } g_i^*(\vec{x}, t) = g^{eq}(\vec{x}, \vec{e}_i, t) \quad (35)$$

$$\text{SchemeD : } g_i^*(\vec{x}, t) = 0. \quad (36)$$

Scheme A is a combination of bounce-back rules and a correction, and Scheme B involves the previous nodal value and a correction. Furthermore, Scheme C treats the unknown energy distribution function as the value of the related equilibrium energy distribution function and a correction, and to be more dramatic, Scheme D adopts that  $g^* = 0$ . It will be shown later that in consistent with the observation in Eq. (16), the influences of the adopted thermal boundary condition will be negligible.

### 5.2. Neumann thermal boundary conditions

Another type of thermal boundary conditions is frequently encountered, i.e. temperature gradient  $\partial T/\partial \vec{x}$  is prescribed. For instance, consider a node  $(i, j, k)$  at the top boundary as shown in Fig. 1 and the temperature gradient  $\partial T/\partial y$  is known. The finite-difference three-point scheme is adopted to calculate the temperature  $T_{i,j,k}$ , which can be expressed as,

$$T_{i,j,k} = \frac{2}{3} \frac{\partial T}{\partial y} |_{i,j,k} \Delta y + \frac{4}{3} T_{i,j-1,k} - \frac{1}{3} T_{i,j-2,k} \quad (37)$$

where  $\Delta y$  is the lattice width. After  $T_{i,j,k}$  is obtained, the unknown particle energy distribution functions can be calculated following the same procedure as Dirichlet thermal boundary conditions.

### 5.3. Corner thermal boundary conditions

The above thermal boundary conditions can be easily applied to the corner nodes. For instance, consider the bottom left corner for the D2Q9 model, where the unknown energy distribution functions are  $g_1$ ,  $g_2$ ,  $g_5$ ,  $g_6$ , and  $g_8$ . Therefore, the internal energy density at the node using Eq. (5), in conjunction with Eq. (26), can be expressed as,

$$\rho\varepsilon = g_0 + [g_1^* + \omega_1 G_c] + [g_2^* + \omega_2 G_c] + g_3 + g_4 + [g_5^* + \omega_5 G_c] + [g_6^* + \omega_6 G_c] + g_7 + [g_8^* + \omega_8 G_c] \quad (38)$$

$$\rho\varepsilon^* = g_0 + g_1^* + g_2^* + g_3 + g_4 + g_5^* + g_6^* + g_7 + g_8^* \quad (39)$$

$$G_c = \frac{\rho\varepsilon - \rho\varepsilon^*}{\omega_1 + \omega_2 + \omega_5 + \omega_6 + \omega_8}. \quad (40)$$

The temperature  $T$  is required to solve for the corner node first, and then the corresponding internal energy  $\varepsilon = D_0 RT/2$  can be calculated with  $D_0 = 2$ . It should be noted that  $g_6$  and  $g_8$  do not stream in and out of the domain. Thus, for Scheme A, the bounce-back values are obtained by extrapolation. Therefore, for simplicity, Scheme B to Scheme D can be generally adopted in the corner.

## 6. Numerical results

### 6.1. 2D thermal Poiseuille flow

Fully developed flow in a channel is a typical case to examine the accuracy of boundary conditions. Here, the 2D Poiseuille flow with constant wall temperature  $T_t$  is considered. The Reynolds number is defined as  $Re = U_0 H/\nu = 10$  in a channel of height  $H$ , and  $U_0$  is the maximum velocity. The effect of viscous heat dissipation is controlled by the Prandtl number  $Pr = \nu/\chi$ . The pressure gradient is set as  $\partial p/\partial x = -8\rho\nu U_0/H^2$ . The analytical solutions for the dynamic and temperature field and the maximum relative error are defined as,

$$U_{exact} = U_0 \left(1 - \frac{y^2}{L^2}\right) \quad (41)$$

$$Err_{max} = \max \left( \frac{\sqrt{(u - U_{exact})^2}}{U_0} \right) \quad (42)$$

$$T_{exact}(y) = T_t + \frac{1}{3} Pr U_0^2 \left[ 1 - \left( \frac{2y}{H} - 1 \right)^4 \right] \quad (43)$$

$$Err_{max} = \max \left( \frac{\sqrt{(T - T_{exact})^2}}{T_t} \right). \quad (44)$$

Velocity boundary conditions and the proposed Dirichlet thermal boundary conditions are applied along the channel walls. Mixed pressure–velocity boundary conditions and periodic thermal boundary conditions are used at the channel inlet and outlet. For the dynamic field, as indicated earlier,  $f_i^*(\vec{x}, \vec{e}_i, t) = f_i(\vec{x}, -\vec{e}_i, t)$  is adopted.

Four different lattice densities in the  $y$  direction are adopted, (33, 65, 129, and 257). Figs. 2 and 3 show the predicted velocity profiles and the second order accuracy is achieved. This is consistent with the accuracy of Eq. (13). It should be noted that other forms of  $f_i^*(\vec{x}, t)$  produce exactly the same results. No slip boundary condition is also satisfied, as indicated in Eq. (14), and this is also independent of the grid spacing, i.e. discrete effect free. If the pressure gradient is treated as a source term and periodic boundary conditions are adopted, then exact solution is obtained with an error less than  $10^{-10}$ . Also, Fig. 4 shows the temperature profiles in comparison with the analytic solution for different Prandtl numbers. Fig. 5 shows that the predicted results are slightly higher than second order accurate for the Prandtl numbers investigated. This is due to the periodic boundary conditions adopted for the energy equation. It is also interesting to note that the differences among the three thermal boundary conditions A, B, and C are negligible. The result adopting Scheme D at higher Prandtl number is also the same and will not be repeated in subsequent computations, except in 2D flow with wall injection. This is consistent with the previous findings in [15,16] for the hydrodynamics flows and is consistent with Eq. (16).

### 6.2. 2D thermal Couette flow

Next, attention is directed to the 2D thermal Couette flow. This is to examine the validity of the proposed thermal boundary conditions at moving wall. Here, the channel top wall is moving at a constant velocity  $U_t$  with a higher constant temperature  $T_t$ , and the bottom wall is stationary with a lower constant temperature  $T_b$ . The Reynolds number is defined as  $Re = U_t H/\nu$  in a channel of height  $H$ . The major control parameters are the Prandtl number and the Eckert number  $Ec = U_t^2/(C_p \Delta T)$ , where  $\Delta T$  is the temperature difference between the hot and cold walls. The effect of viscous heat dissipation

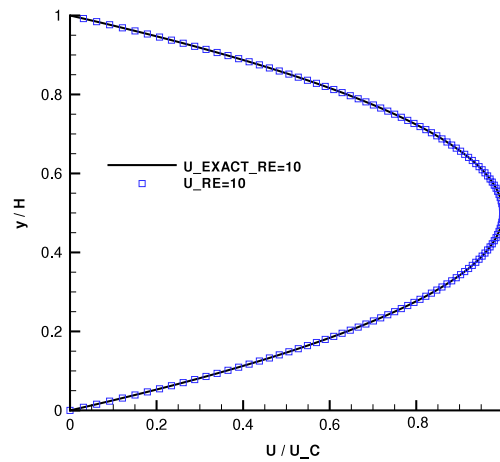


Fig. 2. The velocity profile of a 2D Poiseuille flow.

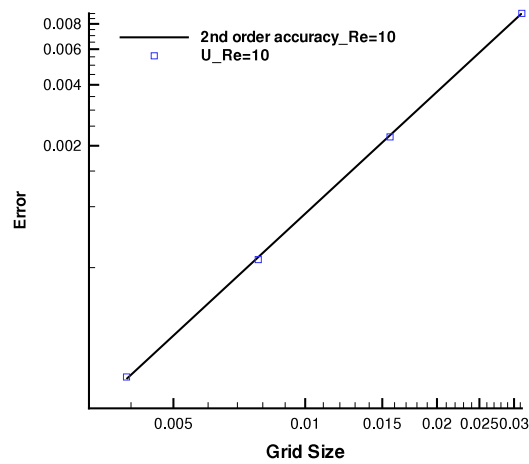


Fig. 3. Maximum predicted velocity relative errors of a 2D Poiseuille flow.

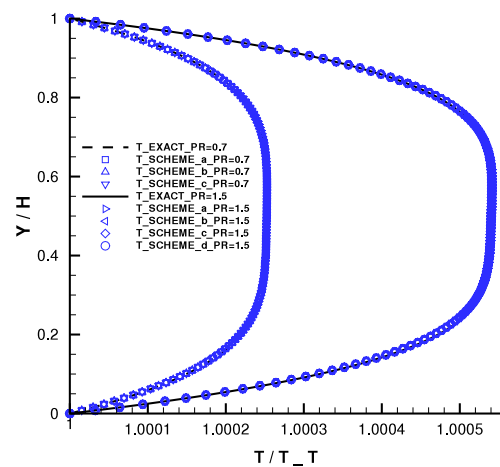


Fig. 4. The temperature profiles of a 2D Poiseuille flow.

is controlled by the Brinkman number  $Br = PrEc$ . The analytical solution for this temperature field is expressed as,

$$T_{\text{exact}}(y) = T_b + \frac{y}{H} \left[ 1 + 0.5Br \left( 1 - \frac{y}{H} \right) \right] \Delta T. \quad (45)$$



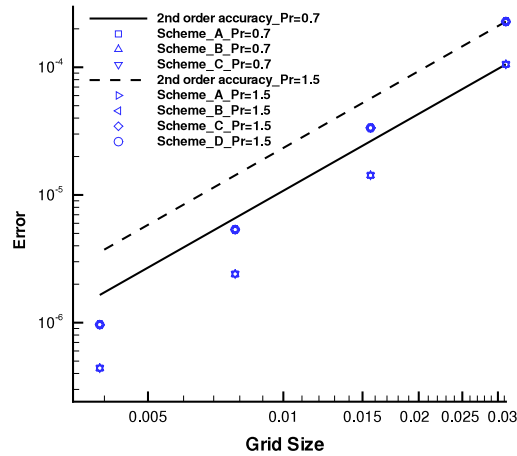


Fig. 5. Maximum predicted temperature relative errors of a 2D Poiseuille flow.

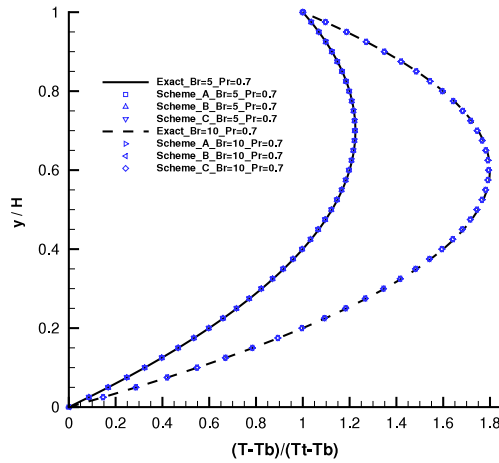


Fig. 6. The temperature profiles of a 2D Couette flow.

Velocity boundary conditions and the proposed Dirichlet thermal boundary conditions are applied along the channel walls, and the periodic boundary condition is applied at the inlet and outlet. Fig. 6 shows the temperature profiles in comparison with the analytic solution for different Brinkman numbers while the Prandtl number is fixed. Five different lattice densities in the  $y$  direction are adopted, (21, 41, 81, 161, and 321), to determine the convergence rate in space. Fig. 7 shows the predicted maximum relative errors and the second order accuracy is achieved.

### 6.3. 2D thermal Couette flow with wall injection

Different from above two simulations, the effects of viscous heat dissipation and compression work done by the pressure are assumed to be neglected in this simulation. Here, the channel top wall is moving at a constant velocity  $U_t$  with a higher constant temperature  $T_t$ , and the bottom wall is stationary with a lower constant temperature  $T_b$ . Fluid is injected from the bottom wall into the channel and extracted from the top moving wall with a vertical component  $V_0$ . The major control parameters are the Prandtl number and the Reynolds number defined based on the injection velocity  $V_0$  and channel height  $H$ , i.e.  $Re = V_0 H / \nu$ . The analytical solutions for the dynamic and thermal field are shown below:

$$U_{exact} = U \left( \frac{e^{(Re y/L)} - 1}{e^{Re} - 1} \right)$$

$$T_{exact}(y) = T_b + \left( \frac{e^{PrRe y/H} - 1}{e^{PrRe} - 1} \right) \Delta T. \quad (46)$$

Velocity boundary conditions and the proposed Dirichlet thermal boundary conditions are applied along the channel walls, and periodic boundary conditions are applied at the inlet and outlet. Five different lattice densities in the  $y$  direction are adopted, (21, 41, 81, 161, and 321), to determine the convergence rate in space.

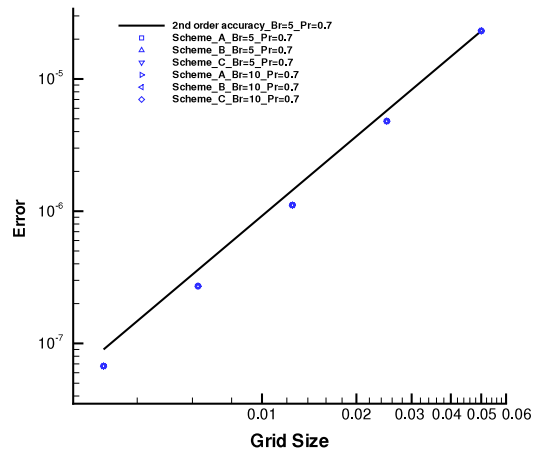


Fig. 7. Maximum predicted temperature relative errors of a 2D Couette flow.

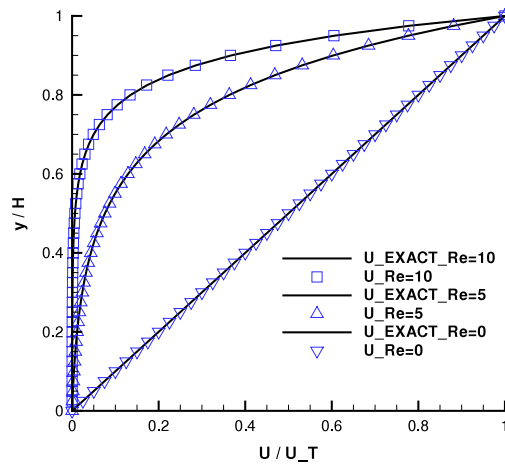


Fig. 8. The velocity profile of a 2D Couette flow with wall injection.

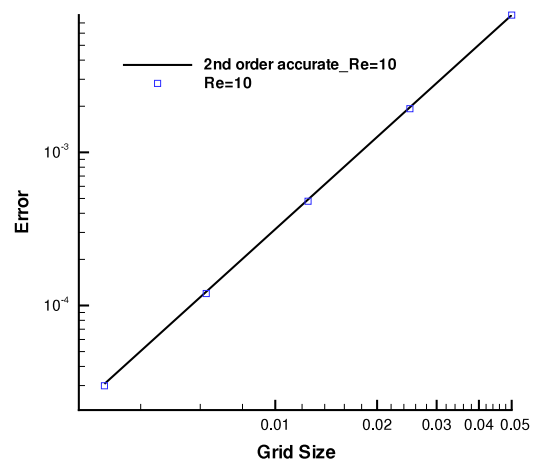


Fig. 9. Maximum predicted velocity relative errors of a 2D Couette flow with wall injection.

The influence of the injection velocity can be observed at high Reynolds number case as shown in Fig. 8, where at the bottom wall the flow is obstructed by the inward jet. Also, Fig. 9 shows the predicted velocity maximum relative errors are second order accurate for the Reynolds numbers investigated. For  $Re = 10$ , Scheme D is also explored. The temperature profiles compared with analytic solution are shown in Fig. 10 and the maximum relative errors using different lattices for

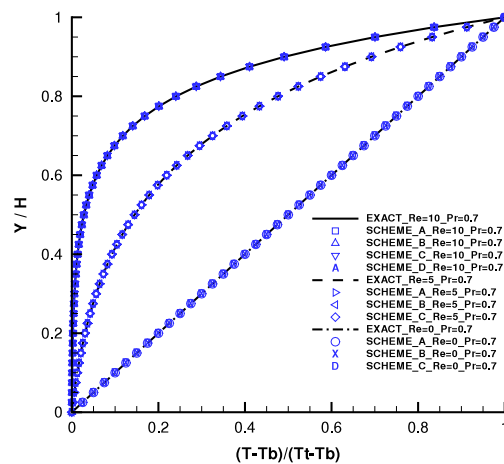


Fig. 10. The temperature profiles of a 2D Couette flow with wall injection.

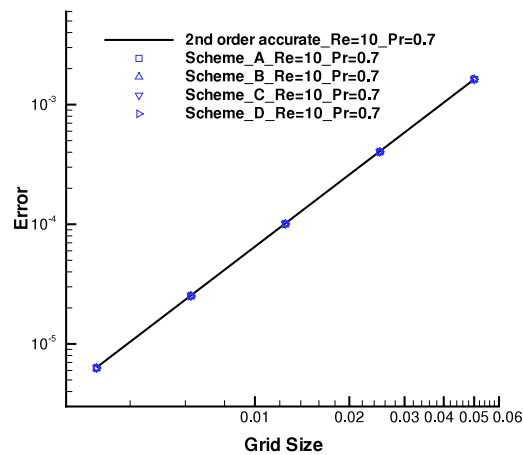


Fig. 11. Maximum predicted temperature relative errors of a 2D Couette flow with wall injection.

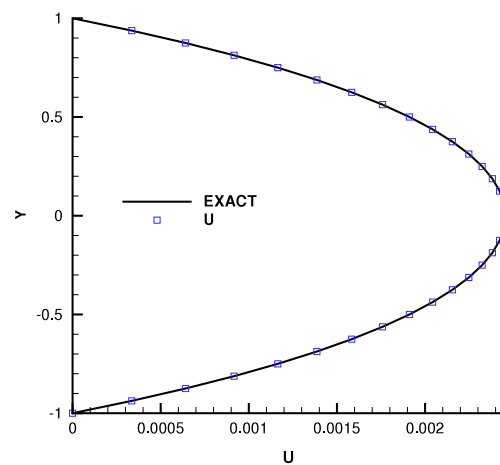


Fig. 12. The velocity profile of a 3D Poiseuille flow in a square duct at  $x/L = 0.5$ .

$Re = 10$  are shown in Fig. 11, which indicates second order accuracy. Again, it is also noted that the differences among the thermal boundary conditions are negligible as expected.

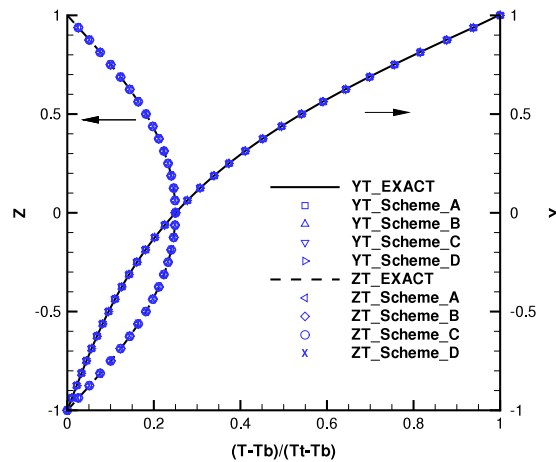


Fig. 13. The temperature profiles of a 3D Poiseuille flow in a square duct.

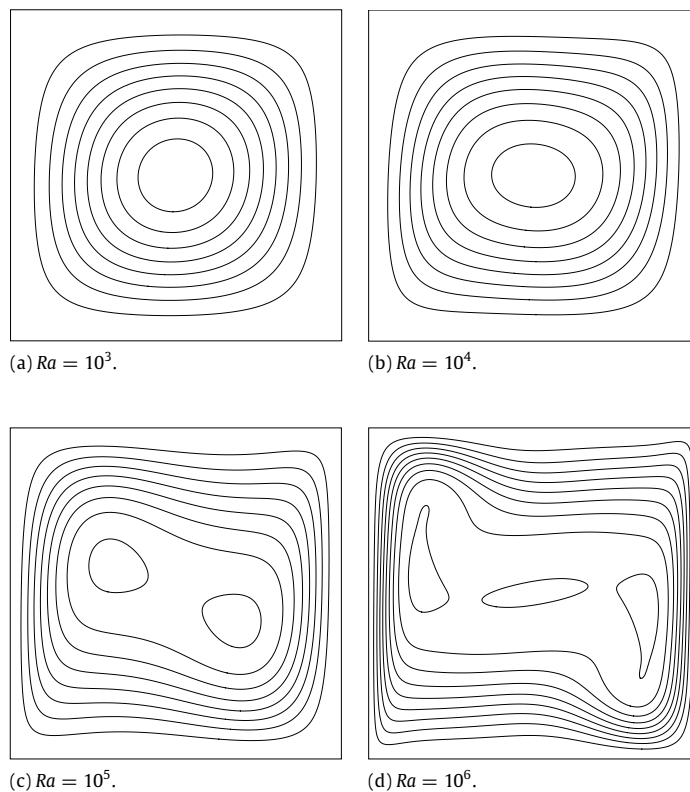
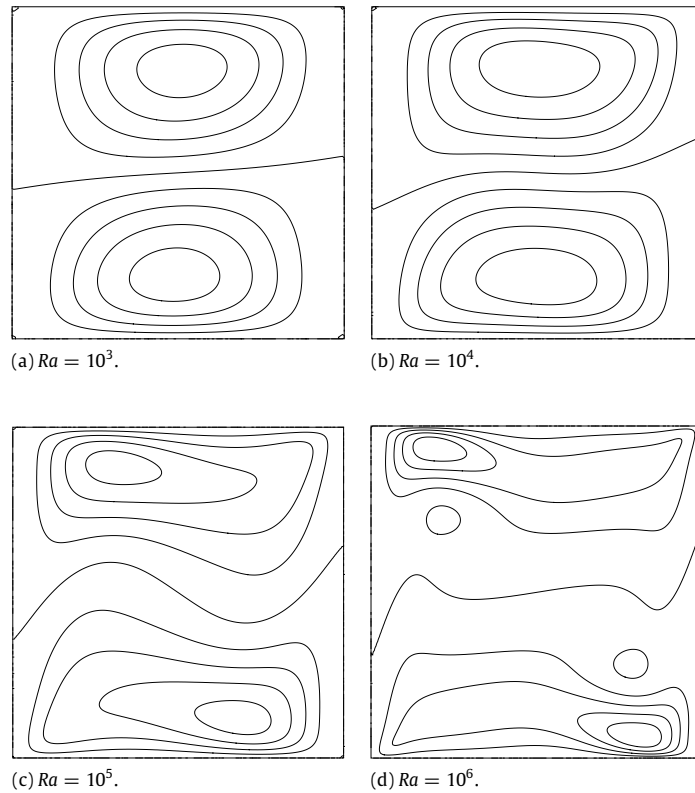


Fig. 14. The streamline profiles of a 2D natural convection in a square cavity at different Rayleigh numbers. (a)  $Ra = 10^3$ ; contours at 1.1(0.11)0; (b)  $Ra = 10^4$ ; contours at 5.0(0.5)0; (c)  $Ra = 10^5$ ; contours at 9.85(0.985)0; (d)  $Ra = 10^6$ ; contours at 15.8(1.58)0.

#### 6.4. 3D thermal Poiseuille flow in a square duct

Here, the capability of the proposed thermal boundary conditions to model 3D problems is examined. It should be noted that Eqs. (14) and (16) are valid for solution with one inhomogeneous direction. Thus, the present case with two inhomogeneous directions provides a good test to validate the assertion that LBM predicts no slip condition across the boundary provided the boundary unknown distribution functions satisfy the macroscopic condition.

A pressure driven 3D square duct flow with different wall temperatures is simulated by the D3Q19 model. Mixed pressure–velocity boundary conditions and periodic thermal boundary conditions are applied at the duct inlet and outlet boundaries. No slip condition and Dirichlet thermal boundary conditions ( $T_t$  at  $y = H$  and the rest of the walls are at  $T_b$ ) are



**Fig. 15.** The horizontal velocity profiles of a 2D natural convection in a square cavity at different Rayleigh numbers. (a)  $Ra = 10^3$ ; contours at  $-3.637(0.7274)3.637$ ; (b)  $Ra = 10^4$ ; contours at  $-16.00(3.200)16.00$ ; (c)  $Ra = 10^5$ ; contours at  $-43.59(8.719)43.59$ ; (d)  $Ra = 10^6$ ; contours at  $-125.5(25.10)125.5$ .

imposed along the bounding walls. The corner treatment is similar to its 2D flow counterpart and is not repeated here. The size of the square duct is  $0 \leq x \leq L$ ,  $-H \leq y \leq H$  and  $-H \leq z \leq H$ , where  $L$  and  $H(=1)$  are duct length and half of the duct height, with  $x$  being the flow direction. The lattice size is  $N_x \times N_y \times N_z$ :  $5 \times 33 \times 33$ . The analytic velocity and temperature profiles are expressed as, [22],

$$u(y, z) = \frac{16H^2}{\mu\pi^3} \left( -\frac{dp}{dx} \right) \sum_{i=1,3,5,\dots}^{\infty} (-1)^{(i-1)/2} \left[ 1 - \frac{\cosh(i\pi z/2H)}{\cosh(i\pi/2)} \right] \frac{\cos(i\pi y/2H)}{i^3} \quad (47)$$

$$\frac{T(y, z) - T_b}{T_t - T_b} = \sum_{i=1,3,5,\dots}^{\infty} \frac{4}{i\pi} \frac{\sinh \frac{i\pi(y+H)}{2H}}{\sinh i\pi} \sin \frac{i\pi(z+H)}{2H}. \quad (48)$$

Figs. 12 and 13 show the velocity and temperature profiles compared with the analytic solution along the vertical and horizontal wall bisectors. Again, the differences of the adopted thermal boundary conditions are negligible.

### 6.5. 2D natural convection in a square cavity

Natural convection in a square cavity is also widely adopted to examine the accuracy of the numerical schemes, where the flow is bounded by a stationary square enclosure with sidewalls maintained at different temperatures and driven by the buoyancy force. For laminar convection in this flow configuration, the viscous heat dissipation is assumed to be negligible. The temperature difference between the walls introduces a temperature gradient in the fluid, and the consequent density difference induces a convective fluid motion. The left wall is at the higher uniform temperature  $T_l$  and the right wall is at the lower uniform temperature  $T_r$ . Both the top and bottom walls are adiabatic, i.e.  $\partial T/\partial y = 0$ .

With the Boussinesq approximation, the buoyancy term is assumed to depend linearly on the temperature as,

$$\rho \vec{G} = \rho \beta \mathbf{g} (T - T_m) \vec{j} \quad (49)$$

where  $\beta$  is the thermal expansion coefficient,  $\mathbf{g}$  is the acceleration due to gravity,  $T_m = (T_l + T_r)/2$  is the average temperature, and  $\vec{j}$  is the vertical direction opposite to that of gravity. To account for this Buoyancy induced force, an extra forcing term

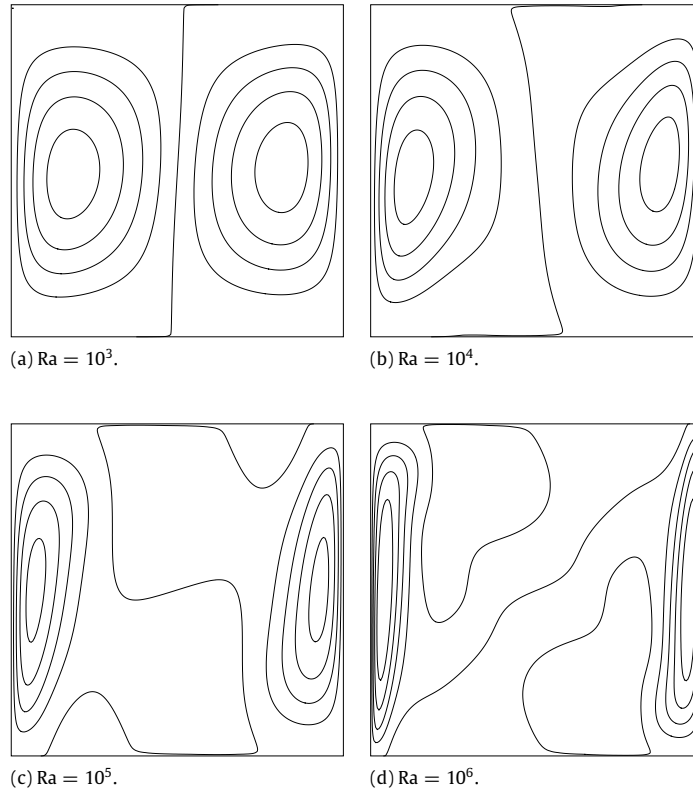


**Fig. 16.** The vertical velocity profiles of a 2D natural convection in a square cavity at different Rayleigh numbers. (a)  $Ra = 10^3$ ; contours at  $-3.663(0.7327)3.663$ ; (b)  $Ra = 10^4$ ; contours at  $-19.39(3.877)19.39$ ; (c)  $Ra = 10^5$ ; contours at  $-67.96(13.59)67.96$ ; (d)  $Ra = 10^6$ ; contours at  $-207.6(41.52)207.6$ .

$F_i$  is added to Eq. (1) and is expressed as [10],

$$F_i = 3\omega_i \frac{\vec{G} \cdot \vec{e}_i}{C}. \quad (50)$$

Other forms of forcing term accounted for the discrete effect could also be adopted [23]. It is noted that the compressibility may influence the results, and this can be eliminated by incompressible model [24]. However, since the present Mach number is low, therefore this influence could be neglected [8].

The major control parameter is the Rayleigh number  $Ra = \beta g \Delta TH^3 Pr / \nu^2$  associated with the heat transfer within the fluid, where  $H$  is the height or width of the cavity. The Nusselt number is also an important dimensionless parameters in describing the convective heat transport. Its average in the whole flow domain is defined as,

$$\overline{Nu} = \frac{H}{\chi \Delta T} \frac{1}{H^2} \int_0^H \int_0^H q_x(x, y) dx dy \quad (51)$$

where  $q_x(x, y) = uT(x, y) - \chi \partial T(x, y) / \partial x$  is the local heat flux in horizontal direction.

Velocity boundary conditions are applied to all boundaries for modeling the flow field, where the domain is covered by a lattice sizes of  $101 \times 101$ ,  $151 \times 151$ ,  $201 \times 201$ , and  $251 \times 251$ , respectively for  $Ra = 10^3$ ,  $10^4$ ,  $10^5$  and  $10^6$ . The proposed Dirichlet thermal boundary conditions are applied at the left and right walls, and the proposed Neumann thermal boundary conditions are applied at the top and bottom walls. Table 1 shows the numerical results of the maximum horizontal velocity on the vertical mid-plane of the cavity,  $u_{\max}$  and its location  $y$ , the maximum vertical velocity on the horizontal mid-plane of the cavity,  $v_{\max}$  and its location  $x$ , and the average Nusselt number  $\overline{Nu}$  for Rayleigh numbers conducted at  $Ra = 10^3$ ,  $10^4$ ,  $10^5$  and  $10^6$ . Note that the velocity shown in the table is normalized by the reference velocity of  $\chi/H$ . Figs. 14–17 show the streamlines, horizontal velocities, vertical velocities, and isotherms at different Rayleigh numbers, respectively. The simulated results are contrasted with the benchmark solutions of De Vahl Davis [25] and the agreements are satisfactory. It is also noted that differences of the predicted velocities and average Nusselt number among four thermal boundary conditions are less than 0.1%. It should also be noted that the convergence rate towards steady state using Scheme B is slower than the other three thermal boundary conditions adopted.

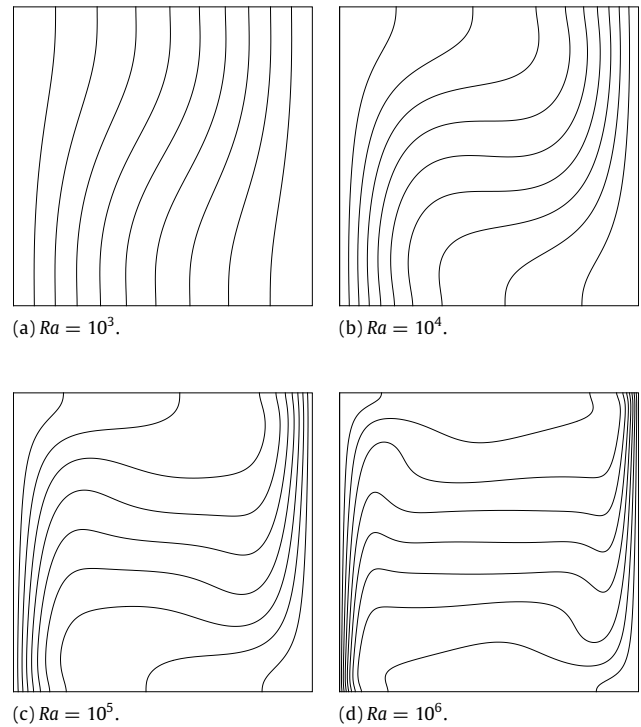


**Fig. 17.** The isotherm profiles of a 2D natural convection in a square cavity at different Rayleigh numbers. (a)  $Ra = 10^3$ ; (b)  $Ra = 10^4$ ; (c)  $Ra = 10^5$ ; (d)  $Ra = 10^6$ ; contours at 1.0(0.1)0 in each case.

**Table 1**  
Comparison of the predicted numerical results and G. De Vahl Davis' benchmark solutions [25] for simulating the 2D natural convection of air in a square cavity.

$Ra$		$10^3$	$10^4$	$10^5$	$10^6$
$u_{\max}$	Davis [25]	3.649	16.178	34.73	64.63
	TBC-A	3.649	16.154	34.508	63.456
	TBC-B	3.648	16.147	34.483	63.443
	TBC-C	3.649	16.148	34.485	63.421
	TBC-D	3.649	16.150	34.489	63.397
$y$	Davis [25]	0.813	0.823	0.855	0.850
	SchemeA	0.810	0.820	0.855	0.848
	SchemeB	0.810	0.820	0.855	0.848
	SchemeC	0.810	0.820	0.855	0.848
	SchemeD	0.810	0.820	0.855	0.848
$v_{\max}$	Davis [25]	3.697	19.617	68.590	219.360
	SchemeA	3.698	19.614	68.595	219.788
	SchemeB	3.696	19.607	68.562	219.697
	SchemeC	3.697	19.608	68.563	219.699
	SchemeD	3.697	19.609	68.564	219.680
$x$	Davis [25]	0.178	0.119	0.066	0.0379
	SchemeA	0.180	0.120	0.065	0.036
	SchemeB	0.180	0.120	0.065	0.036
	SchemeC	0.180	0.120	0.065	0.036
	SchemeD	0.180	0.120	0.065	0.036
$\overline{Nu}$	Davis [25]	1.118	2.243	4.519	8.800
	SchemeA	1.115	2.229	4.489	8.750
	SchemeB	1.115	2.229	4.488	8.750
	SchemeC	1.115	2.230	4.488	8.747
	SchemeD	1.115	2.230	4.488	8.748

## 7. Conclusion

In this paper, consistent thermal boundary conditions for thermal lattice Boltzmann simulations are proposed. The unknown energy distribution functions are made functions of local known energy distribution functions and correctors, where the correctors at the boundary nodes are obtained directly from the definition of internal energy density. In addition, the proposed thermal boundary conditions can be implemented easily for wall and corner boundary using the same formulation. Discrete macroscopic energy equation is derived for a steady and fully developed channel flow, and the resulting equation is second order accurate central difference equation, which also implies that the equation produces continuous energy distribution across the boundary provided the boundary unknown energy distribution functions satisfy the macroscopic boundary energy level. Four different local known energy distribution functions are experimented with to assess this assertion and the applicability of the present formulation, and are examined by computing the 2D thermal Poiseuille flow, thermal Couette flow, thermal Couette flow with wall injection, natural convection in a square cavity, and 3D thermal Poiseuille flow in a square duct. For the cases investigated, second order accurate solutions are obtained, and the differences of the four boundary formulations are as expected negligible, which is consistent with the discrete macroscopic energy equation. Thus, the choice of the local known function can be arbitrary, as long as the macroscopic quantity is satisfied. Also, for simplicity, the thermal boundary condition Scheme C or D could be adopted.

## Acknowledgments

The authors gratefully acknowledge the support by the Taiwan National Science Council (grant 94-2212-E-007-059) and the computational facilities provided by the Taiwan National Center for High-Performance Computing.

## References

- [1] Y.H. Qian, D. d'Humières, P. Lallemand, Lattice BGK model for Navier–Stokes equation, *Europhys. Lett.* 17 (1992) 479.
- [2] S. Chen, G.D. Doolen, Lattice Boltzmann method for fluid flow, *Annu. Rev. Fluid Mech.* 30 (1998) 329.
- [3] D.Z. Yu, R.W. Mei, L.S. Luo, W. Shyy, Viscous flow computations with the method of lattice Boltzmann equation, *Prog. Aerosp. Sci.* 39 (2003) 329.
- [4] G. McNamara, A.L. Garcia, B.J. Alder, Stabilization of thermal lattice Boltzmann models, *J. Stat. Phys.* 81 (1995) 395.
- [5] X. He, S. Chen, G.D. Doolen, A novel thermal model for the lattice Boltzmann method in incompressible limit, *J. Comput. Phys.* 146 (1998) 282.
- [6] P. Lallemand, L.S. Luo, Hybrid finite-difference thermal lattice Boltzmann equation, *Int. J. Modern Phys. B* 17 (2003) 41.
- [7] P. Lallemand, L.S. Luo, Theory of the lattice Boltzmann method: Acoustic and thermal properties in two and three dimensions, *Phys. Rev. E* 68 (2003) 036706.
- [8] Y. Peng, C. Shu, Y.T. Chew, Simplified thermal lattice Boltzmann model for incompressible thermal flows, *Phys. Rev. E* 68 (2003) 026701.
- [9] Y. Shi, T.S. Zhao, Z.L. Guo, Thermal lattice Bhatnagar–Gross–Krook model for flows with viscous heat dissipation in the incompressible limit, *Phys. Rev. E* 70 (2004) 066310.
- [10] X. He, Q. Zou, L.-S. Luo, M. Dembo, Analytic solution of simple flows and analysis of nonslip boundary conditions for the lattice Boltzmann BGK model, *J. Stat. Phys.* 87 (1997) 115.
- [11] D.R. Noble, S. Chen, J.G. Georgiadis, R.O. Buckius, A consistent hydrodynamic boundary condition for the lattice Boltzmann method, *Phys. Fluids* 7 (1995) 203.
- [12] T. Inamuro, M. Yoshino, F. Ogino, A non-slip boundary condition for lattice Boltzmann simulation, *Phys. Fluids* 7 (1995) 2928.
- [13] R.S. Maier, R.S. Bernard, D.W. Grunau, Boundary conditions for the lattice Boltzmann method, *Phys. Fluids* 8 (1996) 1788.
- [14] Q. Zou, X. He, On pressure and velocity boundary conditions for the lattice Boltzmann BGK model, *Phys. Fluids* 9 (1997) 1591.
- [15] C. Chang, C.H. Liu, C.A. Lin, Boundary conditions for lattice Boltzmann simulations with complex geometry flows, *Comput. Math. Appl.* doi:10.1016/j.camwa.2009.02.016.
- [16] C.F. Ho, C. Chang, K.H. Lin, C.A. Lin, Consistent boundary conditions for 2D and 3D laminar lattice Boltzmann simulations, *CMES–Comput. Model. Eng. Sci.* 44 (2009) 137.
- [17] I. Ginzburg, Generic boundary conditions for lattice Boltzmann models and their application to advection and anisotropic dispersion equations, *Adv. Water Resour.* 28 (2005) 1196.
- [18] I. Ginzburg, F. Verhaeghe, D. d'Humières, Study of simple hydrodynamic solutions with the two-relaxation-times lattice Boltzmann scheme, *Comm. Comp. Phys.* 3 (2008) 519.
- [19] A. D'Orazio, S. Succi, C. Arrighetti, Lattice Boltzmann simulation of open flows with heat transfer, *Phys. Fluids* 15 (2003) 2778.
- [20] G.H. Tang, W.Q. Tao, Y.L. He, Thermal boundary condition for the thermal lattice Boltzmann equation, *Phys. Rev. E* 72 (2005) 016703.
- [21] Y. Peng, C. Shu, Y. Chew, A 3D incompressible thermal lattice Boltzmann model and its application to simulate natural convection in a cubic cavity, *J. Comput. Phys.* 193 (2003) 260.
- [22] F.M. White, *Viscous Fluid Flow*, 2nd ed., McGraw-Hill, New York, 1991.
- [23] Z.L. Guo, C.G. Zheng, B.C. Shi, Discrete lattice effects on the forcing term in the lattice Boltzmann method, *Phys. Rev. E* 65 (2002) Article Number: 046308.
- [24] X.Y. He, L.S. Luo, Lattice Boltzmann model for the incompressible Navier–Stokes equation, *J. Stat. Physics* 88 (1997) 927.
- [25] G. De Vahl Davis, Natural convection of air in a square cavity: A bench mark numerical solution, *Internat. J. Numer. Methods Fluids* 3 (1983) 249.